REPORT

ATOMIC PHYSICS

Correlations in high-harmonic generation of matter-wave jets revealed by pattern recognition

Lei Feng*, Jiazhong Hu*, Logan W. Clark, Cheng Chin

Correlations in interacting many-body systems are key to the study of quantum matter. The complexity of the correlations typically grows quickly as the system evolves and thus presents a challenge for experimental characterization and intuitive understanding. In a strongly driven Bose-Einstein condensate, we observe the high-harmonic generation of matter-wave jets with complex correlations as a result of bosonic stimulation. Based on a pattern recognition scheme, we identify a pattern of correlations that reveals the underlying secondary scattering processes and higher-order correlations. We show that pattern recognition offers a versatile strategy to visualize and analyze the quantum dynamics of a many-body system.

High-harmonic generation is an elegant phenomenon in nonlinear optics in which photon populations are transferred to specific excited modes; it enables modern applications such as x-ray sources (*1*), attosecond spectroscopy (*2*, *3*), and frequency combs (*4*, *5*). The generation of high harmonics relies on strong coherent driving and the nonlinearity of the coupling between photons and particles (*6*).

In atom optics, the matter-wave analog of optics, nonlinearity stems from atomic interactions (*7*, *8*). The matter-wave versions of lasers (*9*–*12*), superradiance (*13*–*15*), four-wave mixing (*16*, *17*), Faraday instability (*18*, *19*), and spin-squeezing (*20*, *21*) have made manifest the quantum coherence of matter waves. In particular, a sufficiently strong photon-atom scattering can generate high harmonics of matter waves in superradiant Bose-Einstein condensates (*13*, *15*). Moreover, related experiments on splitting and interfering a condensate (*22*, *23*) have demonstrated and characterized high-order correlations (*24*–*26*), akin to homodyne detection with lasers. Beyond analogies to quantum optics, the manipulation of coherent matter waves can also offer a platform to simulate large-scale (*27*–*29*) and high-energy physics (*30*).

In this work, we demonstrate high-harmonic generation of matter waves by strongly modulating the interactions between atoms in a Bose condensate. Matter waves emerging from the driven condensates form jet-like emission (Bose fireworks) as a consequence of inelastic collisions between atoms (*31*, *32*). Above a threshold in the driving amplitude, bosonic stimulation causes a quantized spectrum of the matter wave. The temporal evolution of the atomic population in the quantized modes suggests a hierarchy of the atomic emission process. By applying a pattern recognition algorithm (*33*, *34*), we identify intriguing second- and higher-order correlations of emitted atoms that are not obvious from individual experiments. Our machine-learning strategy may prove useful for analyzing other complex dynamical systems.

The experiment starts with Bose-Einstein condensates of 60,000 cesium atoms loaded into a uniform disk-shaped trap with a radius of 7 μm, a barrier height of $h \times 300$ Hz in the horizontal direction, and harmonic trapping frequency of 220 Hz in the vertical direction (*31*), where $h = 2\pi\hbar$ is the Planck constant. The interaction between atoms, characterized by the s-wave scattering length a, can be tuned near a Feshbach resonance by varying the magnetic field (*35*).

After the preparation, we oscillate the scattering length as $a(t) = a_{dc} + a_{ac}\sin(\omega t)$ as a function of time t for a short duration of $\tau = 5$ ms with a small dc value $a_{dc} = 3a_0$ and a tunable amplitude a_{ac} at frequency $\omega = 2\pi \times 2$ kHz. Here, a_0 is the Bohr radius. We then perform either in situ imaging or time-of-flight measurement on the sample. At a modulation amplitude $a_{ac} = 25a_0$, we see the emission of matter-wave jets with each atom emitted at a kinetic energy of $\hbar\omega/2$, as evidenced by the velocity with which they leave the sample (*31*).The angles of the emitted jets vary randomly from shot to shot, resulting in a single isotropic ring of atoms after averaging images over many trials (Fig. 1C). At a larger amplitude $a_{ac} = 45a_0$, multiple rings form, labeled as rings 1, 2, and 4 (Fig. 1D). Atoms in each ring have a quantized kinetic energy of $E_j = j\hbar\omega/2 = j\hbar^2 k_f^2/2m$ with the ring number $j = 1, 2$, and 4, where $k_f = \sqrt{m\omega/\hbar}$ is the characteristic wave number of the jets and m is the atomic mass.

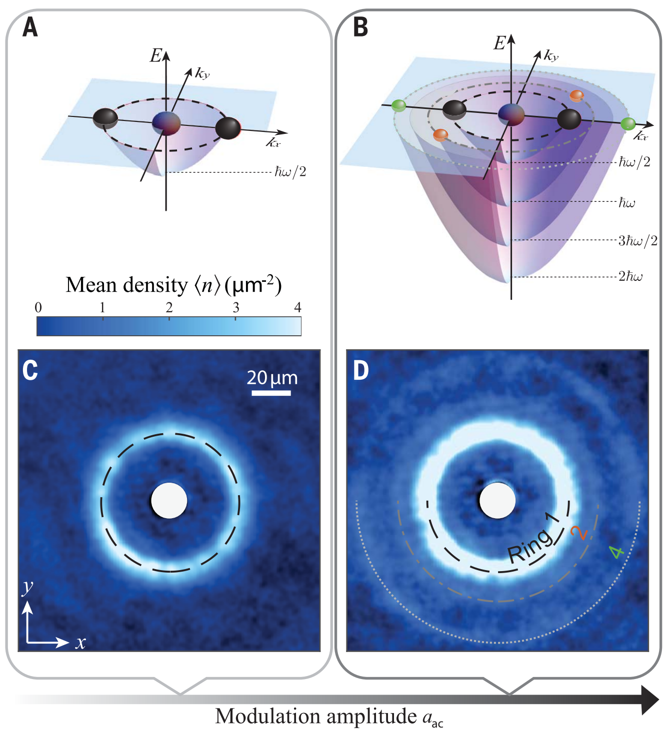

Fig. 1. The first and high-harmonic generation of matter-wave jets in driven condensates. (**A** and **B**) The dispersion relation between energy E and momentum $\hbar\mathbf{k} = \hbar(k_x, k_y)$ in the dressed-state picture. (**C**) The average in situ image of emitted atoms at a small modulation amplitude $a_{ac} = 25a_0$. The emission pattern displays a single ring (highlighted by the black dashed circle), indicating the generation of matter-wave jets with momentum k_f. (**D**) Two more rings (orange and green) in the average image at a larger modulation amplitude $a_{ac} = 45a_0$. Atoms in these three rings have quantized kinetic energies of $\hbar\omega/2$, $\hbar\omega$, and $2\hbar\omega$, respectively. The in situ images are taken at 21 ms after the beginning of the modulation.

James Franck Institute, Enrico Fermi Institute, and Department of Physics, University of Chicago, Chicago, IL 60637, USA.
*Corresponding author. Email: leif1@uchicago.edu (L.F.); hujiazhong01@ultracold.cn (J.H.)

To describe atoms with oscillating scattering length, we write down the Hamiltonian of the system (*36*) as

$$H = \sum_{\mathbf{k}} \varepsilon_{\mathbf{k}} a^{\dagger}_{\mathbf{k}} a_{\mathbf{k}} + \hbar\omega b^{\dagger} b + \sum_{\mathbf{k}_1,\mathbf{k}_2,\Delta\mathbf{k}} \left(A a^{\dagger}_{\mathbf{k}_1+\Delta\mathbf{k}} a^{\dagger}_{\mathbf{k}_2-\Delta\mathbf{k}} a_{\mathbf{k}_1} a_{\mathbf{k}_2} b + \mathrm{h.c.} \right) \quad (1)$$

where $\varepsilon_{\mathbf{k}} = \hbar^2\mathbf{k}^2/2m$ is the kinetic energy of free atoms, $a_{\mathbf{k}}$ ($a^{\dagger}_{\mathbf{k}}$) is the annihilation (creation) operator of an atom with momentum $\hbar\mathbf{k}$, b ($b^{\dagger}$) is the annihilation (creation) operator of photon with an energy of $\hbar\omega$ associated with the magnetic field modulation, A is the coupling strength between atoms and the field, and h.c. is the Hermitian conjugate. The resonant terms that satisfy energy conservation,

$$\varepsilon_{\mathbf{k}_1+\Delta\mathbf{k}} + \varepsilon_{\mathbf{k}_2-\Delta\mathbf{k}} = \varepsilon_{\mathbf{k}_1} + \varepsilon_{\mathbf{k}_2} \pm \hbar\omega \quad (2)$$

describe the dominant collision processes. The momentum and recoil energy of the photon in our experiment are negligible.

The Hamiltonian describes a five-wave mixing process in which, by absorbing or emitting one photon, an atom pair increases or decreases its total kinetic energy by an energy quantum $\hbar\omega$, see Fig. 1, A and B. Here, the phase of the driving field is imprinted to the scattering atoms, distinct from four-wave mixing following a separate pump (*36*). Based merely on the conservation of energy and momentum, the five-wave mixing can produce atoms in a continuous spectrum of energy states. However, given bosonic stimulation, we expect a quantized energy spectrum of the emitted atoms. Starting with the condensate, the collisions first excite atoms to ring 1. As the population in ring 1 builds up, atoms can be further promoted to higher momentum modes through the matter-wave mixing of the condensate and the atoms in ring 1. Because of bosonic stimulation, such a process is dominated by scattering involving three macroscopically occupied modes and the fourth unoccupied mode with higher energy. Therefore, a hierarchy of stimulated collisions is expected. From energy conservation Eq. 2, atoms in the

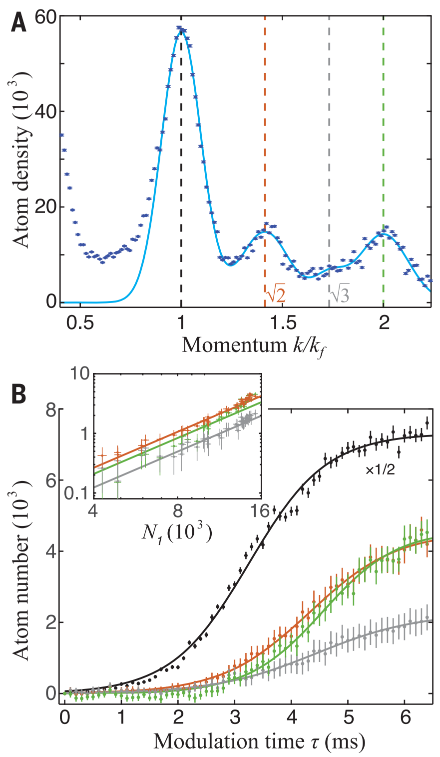

Fig. 2. The atomic population growth in multiple rings. (**A**) A snapshot of the population distribution in momentum space measured by the focused time-of-flight imaging τ = 6 ms after the modulation starts. The cyan curve is a fit to the experimental data for $k/k_f > 0.85$ using a combination of four Gaussians. The vertical dashed lines indicate centers of the Gaussians, fixed at $k/k_f = 1$ (black), $\sqrt{2}$ (orange), $\sqrt{3}$ (gray), and 2 (green), respectively. (**B**) Extracted atom number in each ring as a function of modulation time τ. The atom number in ring 1 (black) is scaled by a factor of ½. Populations in rings 2 (orange), 3 (gray), and 4 (green) start growing after ring 1 is substantially populated. The inset shows the atom number in rings 2, 3, and 4 as a function of the atom number in ring 1 on a log-log scale. The solid lines are the power-law fits to the data with the exponent fixed to 2. The error bars represent one standard error.

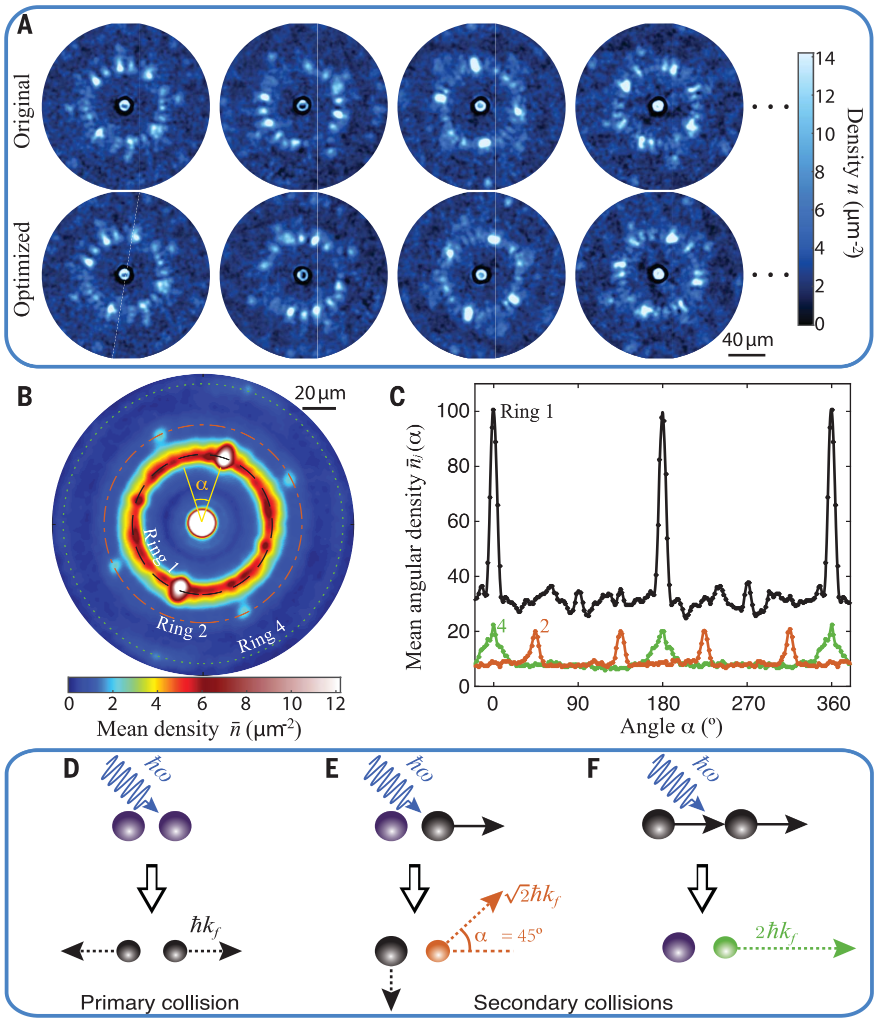

Fig. 3. Pattern recognition and microscopic interpretation. (**A**) Examples from a dataset of 209 raw images (top row). The bottom row shows the corresponding rotated images that maximize the angular variance of the mean image. (**B**) The average of all 209 images after individual rotations, showing the resulting pattern Φ. Besides the bright center spot corresponding to the remnant condensate, 10 more distinct spots emerge in an angular-uniform background: four in ring 1 at α = 0°, 90°, 180°, and 270°; four in ring 2 at α = 45°, 135°, 225°, and 315°; and two in ring 4 at α = 0° and 180°. (**C**) Angular density distributions in rings 1, 2, and 4 extracted from the pattern; the 10 bright spots from (B) show up as peaks in the distributions. (**D** to **F**) Illustrations of microscopic processes that are responsible for the peaks. The purple balls indicate atoms in the condensate. The black, orange, and green balls represent atoms in rings 1, 2, and 4 with momentums of k_f, $\sqrt{2}k_f$, and $2k_f$, respectively.

fourth mode acquire discrete energies $E_j = j\hbar\omega/2$ with j = 2, 3, 4, ..., analogous to the photon spectra from high-harmonic generation.

To verify this picture, we inspect the evolution of the atomic population in each ring using time-of-flight imaging (*29*, *36*). Figure 2A shows an example of the momentum distribution after modulating the scattering length for τ = 5 ms. Besides the distinct peaks at $|\mathbf{k}| = k_f, \sqrt{2}k_f$, and $2k_f$, which are apparent from in situ images (Fig. 1), we also detect a much weaker peak at $|\mathbf{k}| = \sqrt{3}k_f$ (ring 3). We fit the density distribution using a combination of four Gaussians with fixed central positions and widths to extract the population N_j in ring j (*36*).

Populations in all four rings initially show a fast exponential growth and then gradually saturate (Fig. 2B). The population growths of rings 2, 3, and 4 are delayed with respect to that of ring 1. Furthermore, we observe that the populations in higher-order rings are proportional to the square of the population in ring 1, $N_j \propto N_1^2$ with j = 2, 3, and 4 (inset of Fig. 2B). Because the population grows exponentially, this relation is equivalent to $\dot{N}_j \propto N_1^2$, which suggests that the production of atoms in these rings involves two modes in ring 1, in agreement with our model (*36*). We thus consider these processes as secondary collisions that occur after ring 1 is populated by primary collisions.

Beyond the population growth, emissions from secondary collisions display a wealth of intriguing angular structures (Fig. 3A) that are not obvious from the Hamiltonian in Eq. 1 or the average image. To investigate these structures, we use a pattern-recognition algorithm based on unsupervised machine learning. We collect and analyze 209 independent images taken under the same conditions as those in Fig. 1B. We rotate each image by an angle around the center of the condensate iteratively until the angular variance of the mean image is maximized (*36*).

An analysis of the mean image shows a robust and intriguing pattern Φ in the jet emission, containing multiple distinct spots at nonzero momenta on top of angularly uniform rings 1, 2, and 4 (Fig. 3B). These spots arise from a characteristic arrangement of jets that repeatedly appears across many images. Because the condensate has rotational symmetry, instances of this arrangement are randomly oriented in each trial, but the strongest instance in each image is identified and aligned by our algorithm. To better characterize these features, we extract the mean angular density $\bar{n}_j(\alpha)$ for each ring, with α being the relative angle to the brightest spot in ring 1 (Fig. 3C). In this way, we convert the pattern into a series of angular density plots with a flat background and clear peaks representing the spots. This flat background arises from averaging the weaker jets, whose orientations are uncorrelated with the pattern Φ. Because we observe no discernible features from ring 3, in the following we focus on those from rings 1, 2, and 4.

Excluding the uniform background, we find that the concurrence of multiple spots in the pattern points to particular scattering processes populating the corresponding momentum modes. As the first example, two strong peaks in ring 1 (α = 0° and 180°) come from primary collisions of two condensate atoms, which absorb one energy quantum and are scattered into opposite directions with momentum $\pm\hbar k_f$, shown in Fig. 3D.

Following the primary collisions, which are equally likely to emit back-to-back pairs of jets in any direction, strongly stimulated secondary collisions occur that preferentially emit jets in particular directions relative to the primary jets. Although there are many secondary collision processes that satisfy energy and momentum conservation, a small number of them involving three macroscopically occupied modes dominate over others. This is a result of bosonic stimulation, which enhances the rate of scattering processes involving highly occupied modes. The appearance of discrete secondary jets is analogous to optical parametric amplification in a nonlinear medium. These dominant secondary collisions induce eight additional peaks in total among the three rings in the pattern. The four peaks in ring 2 (at α = 45°, 135°, 225°, and 315°) and two peaks in ring 1 (at α = 90° and 270°) arise from the collisions between an atom from ring 1 and another atom from the condensate. One example of such

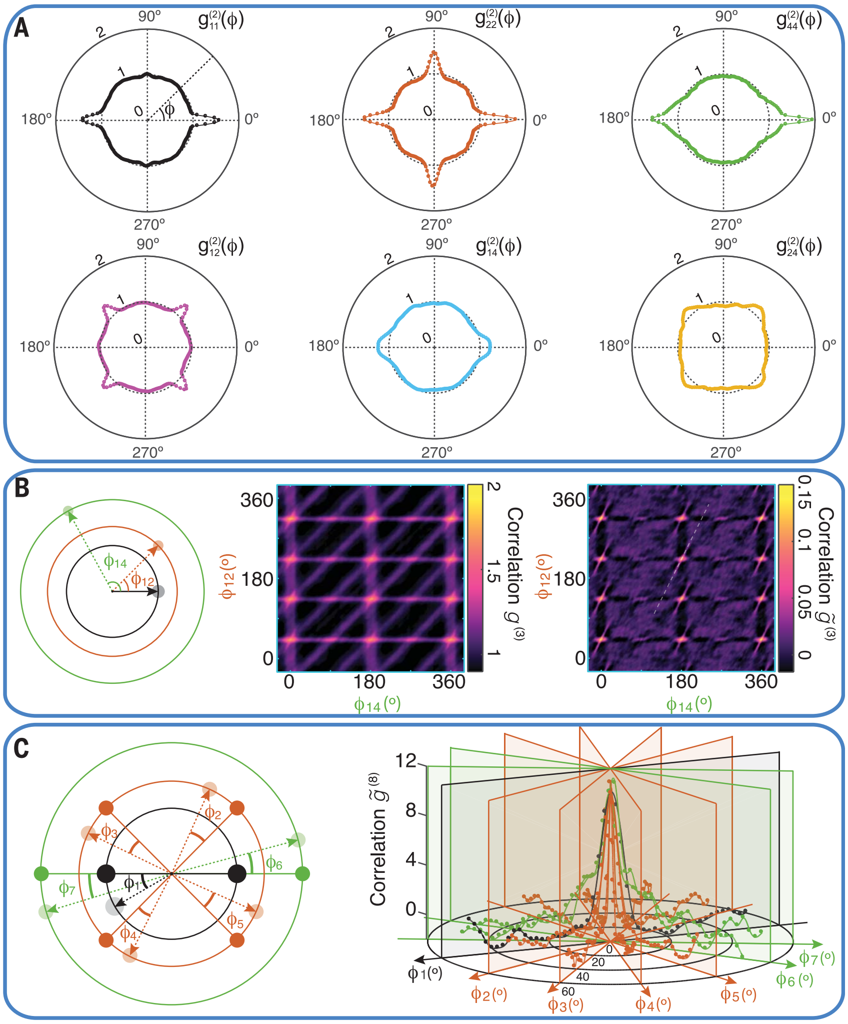

Fig. 4. Second-, third- and eighth-order correlations of emitted matter-wave jets. (**A**) All second-order correlation functions $g^{(2)}_{ij}(\phi)$ within and between rings. (**B**) Third-order correlations $g^{(3)}_{124}(\phi_{12}, \phi_{14})$ and the connected part $\tilde{g}^{(3)}_{124}(\phi_{12}, \phi_{14})$ (center and right panels). Here, ϕ_{12} (ϕ_{14}) are the relative angles between atoms in rings 1 and 2 (4), shown on the left. The extended weak correlations across the peaks in $\tilde{g}^{(3)}_{124}(\phi_{12}, \phi_{14})$ indicate a relation between small angular deviations $\delta\phi_{12} = 2\delta\phi_{14}$ (see the white-dashed line in the right panel as an example). (**C**) Eighth-order connected correlation function $\tilde{g}^{(8)}(\phi_1, \ldots, \phi_7)$ (*36*). We choose a primary jet direction in ring 1 as the reference and show the connected correlation as a function of seven angles relative to the locations of seven bright spots in pattern Φ: one in ring 1 (at 180°; black), four in ring 2 (at 45°, 135°, 225°, and 315°; orange), and two in ring 4 (at 0° and 180°; green). The correlation is shown on seven vertical planes. Within each plane, only one of the seven angles is varied. The connected $\tilde{g}^{(8)}$ reaches 12 and decays rapidly to zero as the angles increase, suggesting a peak in the seven-dimensional space. Solid lines are spline fits to guide the eye.

a collision is illustrated in Fig. 3E, in which a pair of atoms populate two specific modes at α = 45° in ring 2 and at α = 270° in ring 1 by absorbing one photon. This collision process is highly stimulated because it involves three atoms from modes that are already macroscopically occupied; one atom comes from the condensate, and two atoms come from jets produced in primary collisions. Another highly stimulated secondary collision process, shown in Fig. 3F, can explain the origin of the two peaks in ring 4. Here, two copropagating atoms from ring 1 collide; one atom is promoted to ring 4, and the other returns to the condensate. For a detailed comparison of these processes to other possible secondary collisions, see (*36*).

To further support the dominant microscopic collision processes implied by the pattern Φ, we calculate the second-order correlation function $g^{(2)}_{ij}(\phi)$ between momentum modes in rings i and j, namely,

$$g^{(2)}_{ij}(\phi) = \langle n_i(\theta)[n_j(\theta+\phi) - \delta_{ij}\delta(\phi)]\rangle / \langle n_i(\theta)\rangle\langle n_j(\theta+\phi)\rangle \quad (3)$$

Where $n_i(\theta)$ is the angular density in ring i at angle θ, δ_{ij} is the Kronecker delta, and δ(ϕ) is the Dirac delta function. The angle brackets correspond to angular averaging over θ, followed by ensemble averaging over raw images.

All of the second-order correlations involving momenta on the dominant rings display multiple peaks (Fig. 4A). The results are fully consistent with the spots in the pattern Φ and the collisional processes that we identify. In particular, we can associate all the peaks in $g^{(2)}_{22}$ and $g^{(2)}_{12}$ with the process shown in Fig. 3E, in which jets in ring 2 are created at ±45° relative to the primary jets. The peaks in $g^{(2)}_{44}$ and $g^{(2)}_{14}$ are associated with the process in Fig. 3F, in which jets are created along the direction of the primary jets.

We also find four peaks in the cross-correlation between rings 2 and 4. To the best of our knowledge, these correlations cannot come directly from a single secondary collision process. Instead, they could result from the concurrence of two secondary collision processes. Such correlation develops because both processes involve the same macroscopically occupied modes in ring 1 and the condensate.

We further investigate such indirect correlation by calculating the third-order correlation function $g^{(3)}_{124}(\phi_{12},\phi_{14})$ between rings 1, 2, and 4 (Fig. 4B, center), where ϕ_{ij} is the relative angle between emitted atoms in rings i and j (Fig. 4B, left). To remove contributions from the lower-order correlations, we evaluate the connected correlation function $\tilde{g}^{(3)}$ defined as (*26*, *36*)

$$\tilde{g}^{(3)}_{124} = g^{(3)}_{124} - g^{(2)}_{12}(\phi_{12}) - g^{(2)}_{14}(\phi_{14}) - g^{(2)}_{24}(\phi_{24}) + 2 \quad (4)$$

The results are shown in Fig. 4B (right).

The distinct peaks in the connected third-order correlation reveal genuine bunching of the population fluctuations at specific angles in all three rings. In addition, we observe extended weak correlations along lines across the peaks, which relate the angular deviations $\delta\phi_{12} \approx 2\delta\phi_{14}$ (Fig. 4B). We attribute such weak correlations to a Raman-like collision process that couples these three momentum modes by absorbing two energy quanta from the modulation field (*36*).

Beyond third-order correlations, high-harmonic generation can induce even higher-order correlations. An example shown in Fig. 4C is the connected eighth-order correlation. Plotted in the seven-dimensional space spanned by the angular deviations, a prominent peak appears when the angles match the bright spots in our pattern Φ.

Our experiment shows that bosonic stimulation in a driven system can connect different momentum modes in a coherent manner. Although there are other ways to generate high harmonics of matter waves, such as atom-photon superradiance (*13*, *15*) or strong Bragg scattering (*37*), our system is unique in the formation of symmetry-breaking correlations between harmonics by stimulated scattering of matter waves. Our observations introduce a path toward preparing highly correlated systems for applications in quantum simulation and quantum information. In addition, the implementation of pattern recognition can inspire further applications of machine learning to understand complex dynamics of quantum systems.

REFERENCES AND NOTES

1. Z. Chang, A. Rundquist, H. Wang, M. M. Murnane, H. C. Kapteyn, *Phys. Rev. Lett.* **79**, 2967–2970 (1997).
2. M. Hentschel *et al.*, *Nature* **414**, 509–513 (2001).
3. M. Drescher *et al.*, *Science* **291**, 1923–1927 (2001).
4. R. J. Jones, K. D. Moll, M. J. Thorpe, J. Ye, *Phys. Rev. Lett.* **94**, 193201 (2005).
5. C. Gohle *et al.*, *Nature* **436**, 234–237 (2005).
6. R. W. Boyd, *Nonlinear Optics* (Academic Press, ed. 3, 2008).
7. S. L. Rolston, W. D. Phillips, *Nature* **416**, 219–224 (2002).
8. A. D. Cronin, J. Schmiedmayer, D. E. Pritchard, *Rev. Mod. Phys.* **81**, 1051–1129 (2009).
9. M.-O. Mewes *et al.*, *Phys. Rev. Lett.* **78**, 582–585 (1997).
10. B. P. Anderson, M. A. Kasevich, *Science* **282**, 1686–1689 (1998).
11. I. Bloch, T. W. Hänsch, T. Esslinger, *Phys. Rev. Lett.* **82**, 3008–3011 (1999).
12. E. W. Hagley *et al.*, *Science* **283**, 1706–1709 (1999).
13. S. Inouye *et al.*, *Science* **285**, 571–574 (1999).
14. M. G. Moore, P. Meystre, *Phys. Rev. Lett.* **83**, 5202–5205 (1999).
15. D. Schneble *et al.*, *Science* **300**, 475–478 (2003).
16. L. Deng *et al.*, *Nature* **398**, 218–220 (1999).
17. M. Trippenbach, Y. B. Band, P. S. Julienne, *Phys. Rev. A* **62**, 023608 (2000).
18. K. Staliunas, S. Longhi, G. J. De Valcárcel, *Phys. Rev. Lett.* **89**, 210406 (2002).
19. P. Engels, C. Atherton, M. A. Hoefer, *Phys. Rev. Lett.* **98**, 095301 (2007).
20. C. Gross, T. Zibold, E. Nicklas, J. Estève, M. K. Oberthaler, *Nature* **464**, 1165–1169 (2010).
21. M. F. Riedel *et al.*, *Nature* **464**, 1170–1173 (2010).
22. M. R. Andrews *et al.*, *Science* **275**, 637–641 (1997).
23. D. S. Hall, M. R. Matthews, C. E. Wieman, E. A. Cornell, *Phys. Rev. Lett.* **81**, 1543–1546 (1998).
24. V. Guarrera *et al.*, *Phys. Rev. Lett.* **107**, 160403 (2011).
25. R. G. Dall *et al.*, *Nat. Phys.* **9**, 341–344 (2013).
26. T. Schweigler *et al.*, *Nature* **545**, 323–326 (2017).
27. C.-L. Hung, V. Gurarie, C. Chin, *Science* **341**, 1213–1215 (2013).
28. J. Steinhauer, *Nat. Phys.* **12**, 959–965 (2016).
29. L. Feng, L. W. Clark, A. Gaj, C. Chin, *Nat. Phys.* **14**, 269–272 (2018).
30. M. Arratia, *J. Phys. B* 10.1088/1361-6455/aafbb1 (2019).
31. L. W. Clark, A. Gaj, L. Feng, C. Chin, *Nature* **551**, 356–359 (2017).
32. Z. Wu, H. Zhai, arXiv:1804.08251v2 [cond-mat.quant-gas] (27 May 2018).
33. J. Flusser, T. Suk, *Pattern Recognit.* **26**, 167–174 (1993).
34. N. M. Nasrabadi, *J. Electron. Imaging* **16**, 049901 (2007).
35. C. Chin, R. Grimm, P. Julienne, E. Tiesinga, *Rev. Mod. Phys.* **82**, 1225–1286 (2010).
36. See supplementary materials.
37. S. Bernet, M. K. Oberthaler, R. Abfalterer, J. Schmiedmayer, A. Zeilinger, *Phys. Rev. Lett.* **77**, 5160–5163 (1996).
38. L. Feng, J. Hu, L. W. Clark, C. Chin, Correlations in high harmonic generation of matter-wave jets revealed by pattern recognition, Zenodo (2018); doi:10.5281/zenodo.1435185.

ACKNOWLEDGMENTS

We thank B. M. Anderson, K. Levin, Z. Zhang, and M. McDonald for helpful discussions. **Funding:** L.F. is supported by a MRSEC Graduate Fellowship. L.W.C. was supported by a Grainger Graduate Fellowship. This work is supported by the University of Chicago Materials Research Science and Engineering Center, which is funded by the National Science Foundation (DMR-1420709), NSF grant PHY-1511696, and the Army Research Office–Multidisciplinary Research Initiative under grant W911NF-14-1-0003. **Author contributions:** L F. performed the experiment, collected and analyzed data, and wrote the manuscript; J.H proposed and built the models and wrote the manuscript; L.W.C. provided an intuitive theory to explain the experiment; and C.C. supervised the project. **Competing interests:** The authors claim no competing interests. **Data and materials availability:** Published data are available on the Zenodo public database (*38*).

SUPPLEMENTARY MATERIALS

www.sciencemag.org/content/363/6426/521/suppl/DC1
Materials and Methods
Figs. S1 to S4
References (*39–46*)

19 March 2018; accepted 18 December 2018
10.1126/science.aat5008

Science

Correlations in high-harmonic generation of matter-wave jets revealed by pattern recognition

Lei Feng, Jiazhong Hu, Logan W. Clark and Cheng Chin

Science **363** (6426), 521-524.
DOI: 10.1126/science.aat5008

Seeing patterns in atomic jets

Atomic interactions in a Bose-Einstein condensate (BEC) can lead to complex collective behavior. Experimentally, these interactions are often tuned by varying an external magnetic field. Feng *et al.* modulated the interaction among cesium atoms in a BEC. The collisions between atoms exposed to the modulated field sent the atoms flying out of the condensate in jets of seemingly random directions. A pattern-recognition technique revealed that certain directions were associated with particularly large numbers of scattered atoms. The pattern of the scattering maxima could be attributed to secondary collisions.

Science, this issue p. 521